

# Toward High-Fidelity Aerodynamic Shape Optimization for Natural Laminar Flow

Ramy Rashad\* and David W. Zingg†

*University of Toronto, Toronto, Ontario M3H 5T6, Canada*

High-fidelity aerodynamic shape optimization frameworks capable of efficiently incorporating and exploiting laminar-turbulent transition enable the design of aircraft with significantly reduced drag. This work presents recent progress toward that end. First, a two-dimensional Reynolds-averaged Navier-Stokes (RANS) flow solver is extended to incorporate an iterative laminar-turbulent transition prediction methodology. The natural transition locations due to Tollmien-Schlichting instabilities are predicted using the compressible form of the Arnal-Habiballah-Delcourt criterion or alternatively, the simplified  $e^N$  envelope method of Drela and Giles. The boundary-layer properties are obtained directly from the Navier-Stokes flow solution and the transition to turbulent flow is modeled using an intermittency function. The RANS solver is subsequently employed in a gradient-based sequential quadratic programming shape optimization framework. The laminar-turbulent transition criteria are tightly coupled into the objective and gradient evaluations. The gradients are obtained using a parallelized finite-difference approximation. The proposed optimization framework is applied to the lift-constrained drag minimization of airfoils at various flight conditions, leading to natural laminar flow designs.

## I. Introduction and Motivation

THE current push for environmentally responsible aviation requires serious efforts to mitigate the escalating effects of such technology on climate change and natural resources. A clear vision for the efficiency of future transport aircraft – with specific targets for reduced fuel burn, emissions and noise – has been published in the U.S. National Aeronautics Research and Development Plan.<sup>1</sup> As a result, manufacturers and researchers are investigating both conventional and unconventional aircraft designs to meet these targets. As part of the effort to reduce fuel burn and emissions, aerodynamicists are assessing the feasibility of natural laminar flow (NLF) as a key enabler of environmentally responsible commercial aviation.

In the late nineteenth and early twentieth centuries, the breakthrough work of Reynolds and Prandtl began to shed light on the existence, theory, and experimentation of boundary-layers and laminar-turbulent transition.<sup>2</sup> More than a century has passed, and designers have since become heavily reliant on Computational Fluid Dynamics (CFD), as well as single and multidisciplinary design optimization tools. Despite this, there remain few NLF applications in the current commercial fleet, with Honda's recent HA-420 business jet<sup>3</sup> and the nacelles on the recent Boeing 787<sup>4</sup> being among the first, if not the only applications to date. Over the past few decades, the use of CFD under the assumption of fully-turbulent conditions has allowed for stunning advancements in aerodynamic design, but the conservatism leaves something to be desired. Indeed, design tools capable of incorporating and exploiting laminar-turbulent transition enable the design of aircraft with significantly reduced drag.

The lack of NLF applications in the fleet points to the sparsity of available design tools for NLF; it also points to the challenges in reliably realizing extended regions of laminar flow in flight. The transition to turbulence is affected by many factors, including: Reynolds number ( $Re$ ), freestream turbulence intensity

\*PhD Candidate and AIAA Student Member

†Professor and Director, Tier 1 Canada Research Chair in Computational Aerodynamics and Environmentally Friendly Aircraft Design, J. Armand Bombardier Foundation Chair in Aerospace Flight, AIAA Associate Fellow

Copyright © 2013 by Ramy Rashad and David W. Zingg. Published by the American Institute of Aeronautics and Astronautics, Inc. with permission.

( $T_u$ ), pressure gradients, Mach number ( $M$ ), surface roughness and heating, structural noise, rain, hail, icing, and insect impacts.<sup>2,4-6</sup>

Although the preceding list of factors is quite formidable, so are the economic and environmental incentives to investigate the theoretical, experimental, and computational methods that may actualize NLF in commercial aviation. Hence, engineers are exploring a variety of techniques that work to promote laminar flow, including: shaping the aircraft to maintain favourable pressure gradients and lower sweep angles, distributing surface roughness elements to stabilize crossflow instabilities, slat-less wing configurations, boundary-layer suction and wall heating, plasma and piezoelectric actuators, non-stick materials and coatings, and new manufacturing and maintenance procedures. Therefore, the development of design tools capable of efficiently exploiting any of the available techniques are of immediate consequence and benefit.

In this work, NLF design is demonstrated through high-fidelity aerodynamic shape optimization with transition prediction capable of accounting for the effects of  $Re$ ,  $T_u$ ,  $M$ , and the pressure gradients. The Reynolds-averaged Navier-Stokes (RANS) equations are solved using the one-equation Spalart-Allmaras (SA) turbulence model. The solver is first extended to incorporate an iterative laminar-turbulent transition prediction methodology, and is subsequently employed in a gradient-based Sequential Quadratic Programming (SQP) shape optimization framework. The proposed framework presents a good compromise between accuracy, robustness, and efficiency resulting in a flexible, high-fidelity, RANS-based optimization framework for NLF design in subsonic and transonic flight.

## II. Background

### II.A. Transition Prediction in RANS Solvers

The challenges in reliably predicting laminar-turbulent transition continue to limit our ability to predict many aerodynamic flows with accuracy.<sup>7</sup> Consequently, the development of transition prediction methods of varying complexity and fidelity is ongoing. While there are several mechanisms that may lead to transition, the two dominant mechanisms typically encountered in high-speed external aerodynamic flows are Tollmien-Schlichting and crossflow instabilities.<sup>8</sup>

The turbulence models used in RANS solvers do not have the stand-alone capability to predict the laminar-turbulent transition locations in a flow field; in order to predict transition, one must apply a transition criterion. In recent years, several approaches for incorporating transition prediction into RANS solvers have been developed. A review by Arnal *et al.*<sup>9</sup> discusses the various advantages and disadvantages of each approach in detail. The following list attempts to categorize the available strategies:

1. Coupling of a RANS code with a linear or parabolized stability solver and the  $e^N$  criterion.<sup>10-14</sup>
2. Direct implementation of simplified  $e^N$  methods into the RANS code.<sup>6,15-18</sup>
3. Direct implementation of analytical transition onset functions (criteria typically based on  $Re_x$  or  $Re_\theta$ ) into the RANS code.<sup>15-17,19</sup>
4. Coupling of a RANS code with a boundary-layer code and transition prediction using the criteria of methods 1 through 3.<sup>11,20,21</sup>
5. Coupling of additional transport equations to the RANS turbulence model, such as the  $\gamma-Re_\theta$  transition model developed by Langtry and Menter.<sup>22-25</sup> These approaches make use of analytical transition onset functions built into the transport equations.

In the above strategies, the transition criteria employed by the RANS solvers are based on either the  $e^N$  criterion or on transition onset functions. To apply the  $e^N$  criterion one must first approximate the N-factor curves, representing the amplification ratios of the unstable frequencies of the disturbances in the boundary-layer. Transition is assumed to occur when the maximum local N-factor has exceeded some critical value ( $N_{crit}$ ). Values for  $N_{crit}$  must be specified *a priori* based on the freestream turbulence intensity and/or experimental calibration. In computing the N-factor curves, there are several methods of varying fidelity and computational cost. The highest fidelity approach (for RANS solvers) is to solve the parabolized or linearized stability equations at each station to obtain the local N-factors for the unstable frequencies. Simplified approaches have been developed to alleviate the demanding computational cost of such methods, including: the use of database methods generated from linear stability studies, approximating the N-factor envelope through boundary-layer properties (such as the shape factor), and approximating the N-factor

through the pressure gradient and curve fits based on linear stability theory, without the need for boundary-layer properties.<sup>4</sup>

Examples of transition criteria based on a transition onset function are Michel, Granville,  $H-Re_x$ , Abu-Ghannam and Shaw, Gleyzes-Habiballah and Arnal-Habiballah-Delcourt.<sup>15,19,22</sup> These methods have been classified as “simpler” or “analytical” transition criteria.<sup>9</sup> Each have their range of applicability and limitations. These criteria typically compare the boundary-layer properties or related quantities (such as  $Re_\theta$ ) to an empirically calibrated transition onset function (such as  $Re_{\theta_{tr}}$ ). The transition onset functions are typically computed from the integrated boundary-layer properties; the exception being the local transport equation approach developed by Langtry and Menter.<sup>23</sup> The transition point is the first point at which, for example,  $Re_\theta \geq Re_{\theta_{tr}}$ .

In this work, for the prediction of the natural transition locations due to Tollmien-Schlichting instabilities, we employ approaches 2 and 3 from the above list. The boundary-layer properties are computed directly from the Navier-Stokes solution, as described in Section III.A. The framework makes use of Drela’s  $e^N$  envelope method<sup>26</sup> in approach 2, and the relatively new compressible form of the AHD criterion<sup>15</sup> in approach 3; these criteria are presented in Sections III.B and III.C, respectively. Transition prediction is implemented into the RANS solver using an iterative approach, and transition to turbulence is modelled using an explicit intermittency function in conjunction with the SA turbulence model – both are discussed in Section III.D.

Unlike the local  $\gamma-Re_\theta$  transport equation approach,<sup>22</sup> the other approaches are non-local in their formulation, which has some disadvantages. However, these issues are being addressed; for example, approaches 1 and 2 have been successfully parallelized and extended to three-dimensional flows by Krimmelbein *et al.*,<sup>10,27</sup> and there is no restriction to their use in an implicit Newton-Krylov type solver, as demonstrated in this work. There is also no required calibration specific to a particular turbulence model.<sup>24</sup> Furthermore, correlations for crossflow instabilities (such as the  $C_1$  criterion) have already been successfully combined with these approaches, with experimental validation demonstrating accurate transition prediction on transonic swept wings in three dimensions.<sup>16,17</sup> Finally, the modular implementation of the proposed transition prediction framework facilitates the use of higher fidelity methods (such as linear stability theory or the parabolized stability equations) if so desired.

## II.B. RANS-based Aerodynamic Shape Optimization for NLF

Research in the area of high-fidelity aerodynamic shape optimization with laminar-turbulent transition is sparse. The majority of research in this field<sup>5,28–33</sup> employs inviscid-viscous coupling strategies, making use of boundary-layer codes for the viscous formulation and either a panel method or the Euler equations for the inviscid formulation. Although the inviscid/viscous coupling strategies are computationally cheaper than the higher-fidelity RANS solvers, the industry’s trend toward the use of RANS solvers strongly suggests that NLF design tools should follow suit. Recent research making use of RANS solvers to optimize with transition prediction has shown promising results.

Driver and Zingg<sup>21</sup> coupled a RANS optimization framework to the MSES inviscid/viscous solver for transition prediction. This was a stop-gap approach used to successfully demonstrate the potential for NLF design using RANS-based optimization. Lee and Jameson<sup>34</sup> have successfully coupled a RANS solver to a boundary-layer code and an  $e^N$  database method (making use of the Baldwin-Lomax turbulence model) for NLF design in two and three dimensions. Their optimizations focused on the elimination of shock-waves for reduced wave drag. Khayat-zadeh and Nadarajah<sup>35</sup> successfully extended the Langtry-Menter transport equation approach to an adjoint-based optimization framework in two dimensions, and applied the framework to the design of low Reynolds number NLF airfoils with separation bubbles. Design objectives investigated included the minimization of turbulent kinetic energy and the maximization of the lift-to-drag ratio.

There are several specific areas that require continued research and development and have significant room for improvement. The first is the direct use of high-fidelity RANS solvers as opposed to inviscid/viscous coupling strategies. The second is to optimize at higher Reynolds and Mach numbers (representative of subsonic and transonic transport aircraft). A third is to optimize for more realistic and practical designs through the use of multipoint design optimizations that incorporate the off-design performance during the optimization cycle.<sup>36</sup> In the same vein, design objectives and constraints should aim to reflect the industry’s aerodynamic design objectives. Often, design objectives are formulated specifically or primarily to delay transition. Design objectives based on indirect functions – such as N factor curves – run the risk of creating a gap between the design tool’s capabilities and the actual objectives of manufacturers. Finally, in order to account for three-dimensional features such as sweep angle, taper ratio, and twist,<sup>35</sup> there is a need for

continued development of NLF design tools applicable to full aircraft configurations in three dimensions. Ultimately, such design tools should include the prediction of transition due to crossflow instabilities, and they should incorporate the transition criteria into the evaluation of the objective, constraints and gradients of the design problem.

### III. Flow Solver Methodology

The steady RANS equations are solved in two dimensions using a second-order Newton-Krylov finite-difference flow solver (named Optima2D) originally developed by Nemeć and Zingg.<sup>37,38</sup> The linear system that arises at each Newton iteration is solved using the preconditioned Generalized Minimum Residual (GMRES) method. Global convergence of the Newton method is made possible by an approximate factorization startup algorithm. Numerical dissipation is added by either the scalar dissipation scheme of Jameson *et al.*<sup>39</sup> or the matrix dissipation scheme of Swanson and Turkel.<sup>40</sup> The turbulent eddy viscosity is computed using the one-equation Spalart-Allmaras (SA) turbulence model.<sup>41</sup> As mentioned, the SA model is not itself capable of predicting transition; the remaining constituents of the proposed transition prediction framework include: the determination of the boundary-layer edge and properties, the calculation and evaluation of the AHD and  $e^N$  transition criteria, and the implementation of a robust iterative procedure for transition prediction in the RANS solver.

#### III.A. Calculation of the Boundary-Layer Edge

Many transition prediction methods for wall-bounded flows make use of boundary-layer properties. By definition, the various boundary-layer properties are non-local, since they require the integration of flow quantities from the wall to the boundary-layer edge. For example, the AHD criterion requires the calculation of the displacement thickness ( $\delta^*$ ), momentum thickness ( $\theta$ ), shape-factor ( $H$ ), and Pohlhausen number ( $\Lambda$ ), all of which require the calculation of the boundary-layer thickness ( $\delta$ ).

For arbitrary pressure distributions the edge velocity,  $U_e$ , is not known *a priori*. Hence, we must somehow define the boundary-layer edge based on the RANS flow solution. One approach is to couple the RANS solver to a boundary-layer solver that provides a boundary-layer thickness as part of the solution process.<sup>11,20,21,34</sup> The benefit of using a boundary-layer solver is in the accurate calculation of the boundary-layer thickness while allowing for coarser grids to be used in the RANS solver.<sup>11</sup> The disadvantages of the coupling approach include: (i) redundancy in solving both the NS and boundary-layer equations, (ii) restriction to fully-attached and mildly separated flows, (iii) implementation and convergence issues in coupling the two solvers, and (iv) complexities when moving to compressible flows, wings of finite span, and parallel implementations. For these reasons, this work makes use of the available RANS solution, altogether avoiding the use of a boundary-layer solver.

We consider three boundary-layer edge-finding methods; a comparison and assessment of their accuracy may be found in Section V.A. The methods are briefly summarized as follows:

**Compressible Bernoulli Equation:** Following Nebel *et al.*,<sup>14</sup> the first method makes use of the local wall pressure,  $p_w$ , to approximate the edge velocity via the Bernoulli equation for compressible flows,

$$U_e = \sqrt{U_\infty^2 - \frac{2\gamma}{\gamma-1} \frac{p_\infty}{\rho_\infty} \left[ \left( \frac{p_w}{p_\infty} \right)^{\frac{\gamma-1}{\gamma}} - 1 \right]}. \quad (1)$$

The boundary-layer thickness for the given streamwise station, is then searched in the off-wall direction for the point  $\delta=y$  at which  $U=0.99U_e$ , where  $y$  is used here to denote the normal off-wall distance.

**Baldwin-Lomax Diagnostic Function:** Following Stock and Haase<sup>42</sup> and Nebel *et al.*,<sup>14</sup> the second method makes use of a so-called diagnostic function derived from the Baldwin-Lomax turbulence model. The diagnostic function,

$$F = y^a \left[ \frac{dU}{dy} \right]^b, \quad (2)$$

is first computed and its maximum value in the off-wall direction is searched. The boundary-layer thickness is then computed as  $\delta=\epsilon \cdot y_{\max}$ , where  $y_{\max}=y$  at which  $F=F_{\max}$ . The values of the constants have been determined through numerical and experimental investigation to be  $a_l=3.9$ ,  $b_l=1.0$ , and  $\epsilon_l=1.294$  for laminar boundary-layers, and  $a_t=1.0$ ,  $b_t=1.0$ , and  $\epsilon_t=1.936$  for turbulent boundary-layers.<sup>14</sup>

**Vorticity and Shear-Stress Method:** Following Cliquet and Arnal,<sup>15</sup> the third method makes use of the local vorticity,  $\Omega$ , and an approximation to the total shear stress,  $\tau_{tot}$ . The total shear stress is defined as  $\tau_{tot}=\tau_l + \tau_t$ , where  $\tau_l$  and  $\tau_t$  can be expressed in the following manner:<sup>15</sup>

$$\tau_l = \mu|\Omega| \quad \text{and} \quad \tau_t = \mu_t|\Omega|. \quad (3)$$

The boundary-layer thicknesses based on vorticity and shear stress are then searched in the off-wall direction, such that

$$\delta_\Omega = y \quad \text{at which} \quad |\Omega| = \epsilon_\Omega \cdot |\Omega|_{\max}, \quad (4)$$

and

$$\delta_\tau = y \quad \text{at which} \quad |\tau_{tot}| = \epsilon_\tau \cdot |\tau_{tot}|_{\max}, \quad (5)$$

where  $\epsilon_\Omega=0.001$  and  $\epsilon_\tau=0.015$ . Finally, the boundary-layer thickness is taken as the minimum, such that  $\delta=\min(\delta_\Omega, \delta_\tau)$ .

In Section V.A, an investigation into the accuracy of the integrated boundary-layer properties is considered through a detailed grid convergence study. With the boundary-layer edge defined (facilitating the calculation of the boundary-layer properties) the next step is to consider the evaluation of a transition criterion.

### III.B. AHD Transition Criterion

The natural transition locations (due to Tollmien-Schlichting instabilities) are predicted using the new compressible form of the Arnal-Habiballah-Delcourt (AHD) criterion.<sup>15-17,43</sup> The AHD criterion is designed for low to moderate freestream turbulence intensities ( $T_u \leq 0.1\%$ ), as typically encountered in external aerodynamic cruise conditions for transport aircraft.<sup>15</sup> The method has the advantage of being applicable to a wide range of pressure gradients, as well as compressible flows.<sup>15</sup>

Beginning at the stagnation point, we march toward the trailing edge of the airfoil, treating the upper and lower surfaces independently. Our first task is to find the streamwise location of the neutral stability point,  $s_{cr}$ . Upstream of the neutral stability point, it is assumed (from linear stability theory) that all small disturbances over all frequencies remain stable and damp out. The neutral stability point is found using the *critical* Reynolds number, calculated as a function of the incompressible shape factor,  $H_i$ , as

$$Re_{\theta_{cr}} = \exp \left[ \frac{E}{H_i} - F \right], \quad (6)$$

such that  $s_{cr}$  is the first point at which, locally,  $Re_\theta = Re_{\theta_{cr}}$ . The functions E and F may be found in the Appendix. Note that  $Re_{\theta_{cr}}$  typically decreases in the streamwise direction and is greater than  $Re_\theta$  upstream of the critical point.

The next step is to find the streamwise location of the laminar-turbulent transition point,  $s_{tr}$ . The transition criterion is computed and checked only at points downstream of the neutral stability point. The AHD criterion uses the Falkner-Skan self-similar solutions to represent the laminar boundary-layer profiles, which are characterized by the local Pohlhausen number.<sup>15</sup> Following the work of Granville, the necessary relationships are extended from self-similar boundary-layers to actual flows by replacing  $\Lambda_2$  with its mean value as follows:<sup>15</sup>

$$\Lambda_2 = \frac{\theta^2}{\nu} \frac{dU_e}{ds} \quad \implies \quad \overline{\Lambda_2} = \frac{1}{s - s_{cr}} \int_{s_{cr}}^s \Lambda_2 ds. \quad (7)$$

Arnal *et al.* proposed the following expression for the transitional Reynolds number,  $Re_{\theta_{tr}}$ :

$$Re_{\theta_{tr}} = Re_{\theta_{cr}} + A \cdot \exp(B \cdot \overline{\Lambda_2}) \left[ \ln(C \cdot T_u) - D \cdot \overline{\Lambda_2} \right], \quad (8)$$

where  $T_u$  is the freestream turbulence level, and the functions A, B, C, and D may be found in the Appendix. The transition point is then taken as the first point at which, locally,  $Re_\theta = Re_{\theta_{tr}}$ . Note that  $Re_{\theta_{tr}}$  typically decreases in the streamwise direction and is greater than  $Re_\theta$  upstream of the transition point.

### III.C. Simplified $e^N$ envelope method

The simplified  $e^N$  envelope method used in Drela's XFOIL and MSES codes<sup>26</sup> has also been incorporated. The method makes direct use of the boundary-layer properties to approximate the envelope of the spatial amplification rates of the disturbances (the N-factors), as opposed to actually solving the linear stability equations; while the envelope method does not track individual frequencies, it is significantly more efficient.<sup>18</sup> The correlations are based on linear stability results for the Falkner-Skan family of velocity profiles. The envelopes of the growth rates are locally approximated as straight lines with respect to the streamwise direction,  $\xi$ , as follows:<sup>26</sup>

$$\frac{dN}{d\xi} = \text{fcn}(H_k, \theta) = \frac{dN}{dRe_\theta} \cdot \frac{m+1}{2} \cdot l \cdot \frac{1}{\theta}, \quad (9)$$

where  $\frac{dN}{dRe_\theta}$ ,  $m$ , and  $l$  are functions of the so-called kinematic shape factor,  $H_k$ , and may be found in the Appendix. The kinematic shape factor is computed based on the incompressible shape factor,  $H_i$ , and the Mach number at the boundary-layer edge,  $M_e$ , as

$$H_k = \frac{H_i - 0.290M_e^2}{1 + 0.113M_e^2}. \quad (10)$$

The N-factor envelope is then obtained by integrating Equation (9) in the streamwise direction, beginning at the critical point. The critical point is the first point at which, locally,  $Re_\theta = Re_{\theta_{cr}}$ , where  $Re_{\theta_{cr}}$  is defined by<sup>26</sup>

$$\log_{10} Re_{\theta_{cr}} = \left( \frac{1.415}{H_k - 1} - 0.489 \right) \tanh \left( \frac{20}{H_k - 1} - 12.9 \right) + \frac{3.295}{H_k - 1} + 0.44. \quad (11)$$

### III.D. RANS Implementation

#### III.D.1. Iterative Transition Prediction Procedure

Automatic transition prediction in the RANS solver is achieved through an iterative process, which has been developed by several researchers.<sup>6,11,15,18,20,43</sup> This section provides an overview of the current implementation.

An initial guess of the transition locations (top and bottom surfaces) is required and typically taken at 25% chord. When the magnitude of the flow residual has been reduced to  $5 \times 10^{-6}$ , the transition prediction module is invoked to process the RANS solution; the tight tolerance was chosen to ensure sufficiently accurate boundary-layer properties for transition prediction. The initial guess is then moved upstream or downstream as required toward the newly predicted transition points in an under-relaxed fashion,<sup>20</sup> such that

$$x_{tr}^{\text{new}} = x_{tr}^{\text{old}} - \omega \left( x_{tr}^{\text{old}} - x_{tr}^{\text{predicted}} \right), \quad (12)$$

where  $\omega$  is the under-relaxation factor, and  $x_{tr} = x/c$  represents a normalized chord position. When the flow residual returns to a magnitude of  $5 \times 10^{-6}$ , the transition points are again updated. The iterative transition prediction procedure is considered converged when  $\Delta x_{tr} = |x_{tr}^{\text{new}} - x_{tr}^{\text{old}}|$  has converged to a tolerance of  $\epsilon_{tp}$ . The flow solver then continues to converge – with the final predicted transition locations – until the magnitude of the flow residual has reduced to a tolerance of  $\epsilon_r$ . For the purposes of gradient-based aerodynamic shape optimization,  $\epsilon_{tp}$  and  $\epsilon_r$  are set to  $10^{-6}$  and  $10^{-12}$ , respectively, ensuring a sufficiently smooth design space for optimization.

From numerical experimentation, an under-relaxation factor of  $\omega=0.8$  is used at the outset, increasing to  $\omega=1.0$  when  $\Delta x_{tr} \leq 0.01$ . This was found to be a good compromise between efficiency and robustness. A linear extrapolation of the boundary-layer properties – from the laminar region into the turbulent region – allows the transition criterion to predict transition downstream of the forced transition points (when required). If laminar flow separation is detected, then the separation point is taken as an approximation to the transition point.<sup>11</sup> A robust logic has been determined through extensive numerical experimentation and code verification to handle the various outcomes of the transition prediction module. For the various airfoils and flight conditions investigated, it was found that the iterative transition prediction procedure requires approximately three to four times the computational cost of a fully-turbulent flow solve, with no significant addition to the memory requirements.

### III.D.2. Modelling of Transitional Flow Regions

The transition to turbulence is enforced in the Navier-Stokes solution by one of two methods. The first makes use of the trip term and the  $f_{t_1}$  and  $f_{t_2}$  trip functions in the SA model, as published by Spalart and Allmaras.<sup>41</sup> The second approach makes use of an intermittency function that scales the turbulent eddy viscosity, such that  $\mu_t = \gamma\mu_t$  and  $0 \leq \gamma \leq 1$ , as used by Cliquet *et al.*<sup>15</sup> The intermittency function takes the form of an S-type curve as defined by Krumbein,<sup>44</sup> such that

$$\gamma(x) = 1 - \exp(-0.412 \xi^2), \quad \text{where} \quad \xi = 3.36 \frac{x - x_{\text{tr}}^{\text{beg}}}{l_{\text{tr}}}, \quad (13)$$

$x_{\text{tr}}^{\text{beg}}$  represents the beginning of the transitional flow region as predicted by the transition criterion, and  $l_{\text{tr}}$  is the transition length. Although there are no physics-based methods for determining the transition length,<sup>18</sup> empirically correlated approximations have been developed that make use of the boundary-layer properties at the transition point. Following the work of Krumbein,<sup>44</sup> the transition length can be obtained from

$$Re_{l_{\text{tr}}} = 4.6 (Re_{\delta_{\text{tr}}^*})^{1.5}. \quad (14)$$

For a smooth ramp-up of the eddy viscosity, the transition region must be sufficiently resolved; failure to do so was observed to cause noise in the design space during optimization. A comparison of the eddy viscosity ramp-up using the two transition region models is presented in Section V.D.

## IV. Optimization Framework

The goal of the aerodynamic shape optimization framework is to minimize the specified design objective,  $J$ , with respect to the design variables,  $X$ , subject to linear and nonlinear constraints. Although the optimizer can handle several different design objectives, such as the maximization of lift-to-drag ratio or endurance factor, in this work the focus will be on lift-constrained drag minimization. The proposed optimization framework consists of the following constituents: (i) a two-dimensional RANS flow solver (as described in the preceding section), (ii) a geometry parametrization and mesh movement algorithm, (iii) a sequential quadratic programming algorithm, and (iv) a finite-difference gradient evaluation.

The airfoil geometry is parametrized using B-splines, the details of which may be found in Nemeć and Zingg.<sup>37</sup> The design variables,  $X$ , are defined as the  $y$ -coordinates of the B-spline control points; the control points are free to move in the vertical direction to facilitate shape changes during the optimization cycle. The angle of attack of the airfoil is an additional design variable. The algebraic grid-perturbation strategy described in Nemeć and Zingg<sup>37</sup> is used to ensure that the computational grid is smoothly adjusted to conform to the changing geometric configurations.

The SNOPT general purpose Sequential Quadratic Programming (SQP) algorithm – developed by Gill *et al.*<sup>45</sup> – is employed as the optimizer in this work. SQP methods are among the most effective gradient-based approaches for treating smooth, nonlinearly constrained optimization problems.<sup>46</sup> SNOPT solves problems that are locally optimal by minimizing quadratic models of the augmented Lagrangian.<sup>45</sup> A backtracking line-search strategy is used to determine the step-size and update the design variables in a manner that ensures a sufficient decrease in the augmented Lagrangian merit function. The Hessian of the Lagrangian is approximated using the quasi-Newton method of Broyden, Fletcher, Goldfarb, and Shanno (BFGS). SNOPT requires the gradients of the objective function and constraints; ensuring sufficiently accurate gradients is of paramount importance to the success of the SQP algorithm. The gradients of the objective function and constraints required by SNOPT are found using a finite-difference approximation, as discussed in the following section.

### IV.A. Parallel Finite-Difference Gradient Evaluation

The gradients of the objective and constraint functions with respect to the design variables – the B-spline control points and angle of attack – may be obtained through a finite-difference approximation. In doing so, we can approximate the gradients without having to differentiate the solver. Meanwhile the resulting gradients implicitly contain the sensitivities of the laminar-turbulent transition criterion that defines the transition locations, in turn allowing the optimizer to exploit that information.

The components of the gradient vector,  $G_n$ , are evaluated using a second-order centered-difference approximation as follows:

$$G_n = \frac{J[X + h_n e_n, Q(X + h_n e_n)] - J[X - h_n e_n, Q(X - h_n e_n)]}{2h_n} \quad n = 1, \dots, N_D \quad (15)$$

where  $N_D$  is the number of design variables,  $e_n$  is the  $n^{\text{th}}$  unit vector, and  $h$  is a positive scalar defined as

$$h_n = \max(\epsilon \cdot |X_n|, 10^{-6}). \quad (16)$$

The step-sizes,  $h_n$ , are computed by scaling the magnitude of the design variables,  $|X_n|$ , by the constant  $\epsilon$ . If the step-size used in the approximation of the gradients is too large, the truncation error will dominate and the required accuracy of the gradients will not be attained. If the step-size is too small, subtractive cancellation will introduce significant error.<sup>5</sup> Numerical studies were performed on the NACA-0012 and RAE-2822 airfoils to determine an appropriate order of magnitude for  $\epsilon$ . For both airfoils, it was observed that the gradient components were relatively constant over a range of  $\epsilon$  values from  $10^{-4}$  to  $10^{-2}$ . Hence, a value of  $\epsilon = 10^{-3}$  is used in equation (16) to compute the step-sizes,  $h_n$ , in all optimization cases using the finite-difference gradient evaluation.

The centered-difference approximation requires two flow solves to evaluate each component of the gradient, and as such, it does not scale well with the number of design variables. In this work, the gradient evaluation has been parallelized such that multiple processors compute the necessary flow solves – on the entire set of perturbed geometries – in parallel. The flow solve required on the baseline geometry is also carried out in parallel. For example, a case with eleven design variables would employ twenty-three processors in the parallel computation of the objective and gradients. Thus, one can obtain all of the necessary information in approximately the same turn-around time as a single serial flow solve. Although this approach works well in two dimensions, the required computational resources become prohibitive in three dimensions. To address these scaling issues, future work will focus on extending the current transition prediction framework to the discrete adjoint gradient evaluation method.<sup>37</sup>

## V. Results

### V.A. Boundary-Layer Properties

In order to verify the three boundary-layer edge finding methods described in Section III.A, numerical flow solutions using fixed transition locations were computed using the Optima2D flow solver (described in Section III). The results from Optima2D are compared to numerical results obtained from XFOIL, developed by Drela.<sup>26</sup> XFOIL is a two-dimensional, incompressible flow solver which couples an inviscid solver to a viscous boundary-layer code. The inviscid formulation in XFOIL is a linear vorticity-streamfunction panel method. The viscous flow in the boundary-layer and wake is modeled with a two-equation lagged dissipation integral boundary-layer method.<sup>26</sup>

Flow solutions were computed on the NACA-0012 airfoil with a sharp trailing edge at  $Re=1 \times 10^6$ ,  $M=0.20$  and zero incidence, using a C-grid with  $321 \times 384$  nodes. In both solvers, transition was fixed at 50% chord on the top and bottom surfaces of the airfoil. A comparison of the three edge-finding methods in Optima2D is presented in Figure 1(a), along with the edge velocity obtained using XFOIL. The comparison verifies the ability of the various methods to define the boundary-layer edge, without the use of a boundary-layer solver. Good agreement is observed between the methods in Optima2D and XFOIL in both the laminar and turbulent regions, although our interest here is restricted to the laminar region for the purpose of predicting transition.

The accuracy of the integrated boundary-layer properties is assessed through a grid convergence study and by comparison to numerical boundary-layer properties obtained from XFOIL. All results are obtained using matrix dissipation, which is highly recommended for the present purpose to avoid excessive numerical dissipation in the boundary-layer. Figure 1(b) presents a grid convergence study of the boundary-layer shape factor ( $H$ ) for the same NACA-0012 test case. The grid-convergence results shown here were obtained using the vorticity and shear-stress edge-finding method. The numbers in brackets provide the approximate number of nodes in the laminar boundary-layer. These results verify the current implementation and demonstrate that with reasonable grid density, sufficient accuracy of the boundary-layer properties can be computed directly from the Navier-Stokes solution, confirming similar results found by Brodeur and van Dam.<sup>6</sup>

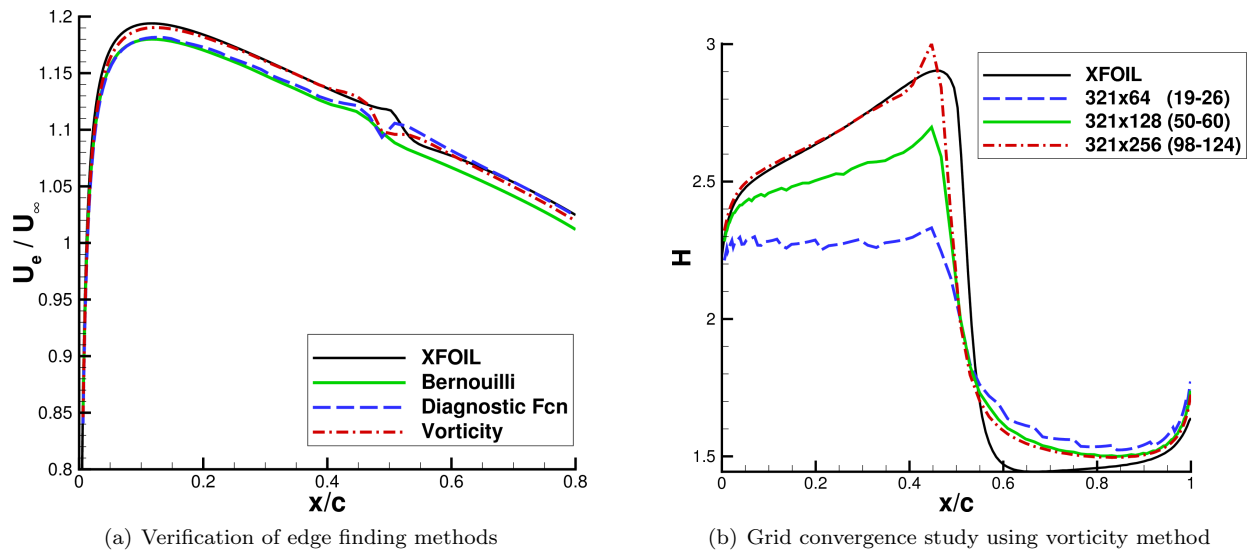


Figure 1. NACA-0012 verification of edge finding methods and boundary-layer properties

### V.B. Transition Prediction

The predictive capability of the transition prediction framework is first verified by comparison to numerical results generated using XFOIL on the NACA-0012 airfoil. The transition prediction in XFOIL makes use of the simplified  $e^N$  envelope method developed by Drela,<sup>26</sup> and thus provides a good benchmark for verification.

In Figure 2, transition prediction results are shown for a  $449 \times 385$  C-grid around the NACA-0012 airfoil at  $Re = 10 \times 10^6$ ,  $M = 0.2$ , and a freestream turbulence intensity ( $T_u$ ) of 0.1% (corresponding to an N-factor of 8 for the  $e^N$  criterion). The Optima2D (O2D) points represent the final converged transition locations using the AHD criterion. Good agreement between XFOIL and Optima2D is observed. The AHD criterion predicts transition upstream of the  $e^N$  envelope method. Similar trends have been found by Cliquet and Arnal<sup>15</sup> and Streit *et al.*<sup>17</sup>

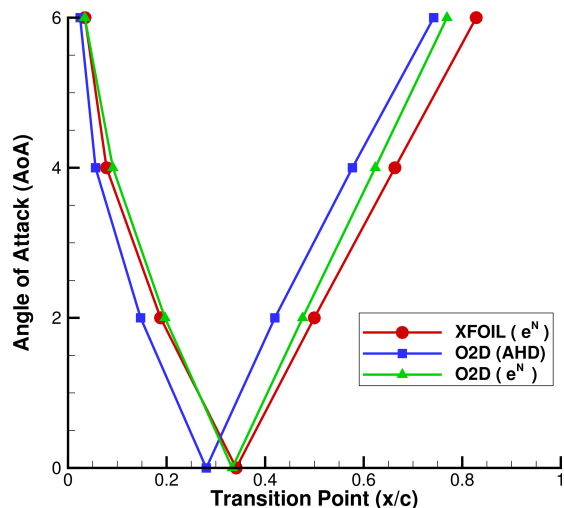


Figure 2. NACA-0012 transition prediction

Validation of the transition prediction framework and the transition criteria has been carried out by comparison to available experimental transition data for the NLF-0416 airfoil developed by Somers.<sup>47</sup> The experimental results were obtained in the Langley Low Turbulence Pressure Tunnel (LTPT) using microphoned pressure taps.<sup>47</sup> The resolution of the experiments corresponds to the physical spacing of the microphoned taps along the chord of the airfoil.

Presented herein are the test case results for a  $449 \times 385$  C-grid around the NLF-0416 airfoil at  $Re = 4 \times 10^6$ ,  $M = 0.2$ , and  $T_u = 0.1\%$  (and  $N = 8$  for XFOIL). The transition points predicted by both Optima2D and XFOIL are presented in Figure 3, along with the wind tunnel experimental data. The results of this test case show that the predictive capabilities of Optima2D match closely with the published experimental results over a range of lift coefficients.

Figure 4 presents the drag polar for the NLF-0416 airfoil using both Optima2D and XFOIL. Good agreement is observed between the experimental results and the drag polars computed using both Optima2D and XFOIL. In Somers' report,<sup>47</sup> the freestream turbulence intensity,  $T_u$ , was unfortunately not published for the NLF-0416 experiments. It is possible that the wind tunnel may have had lower or higher  $T_u$  than the 0.1% used for the computations.

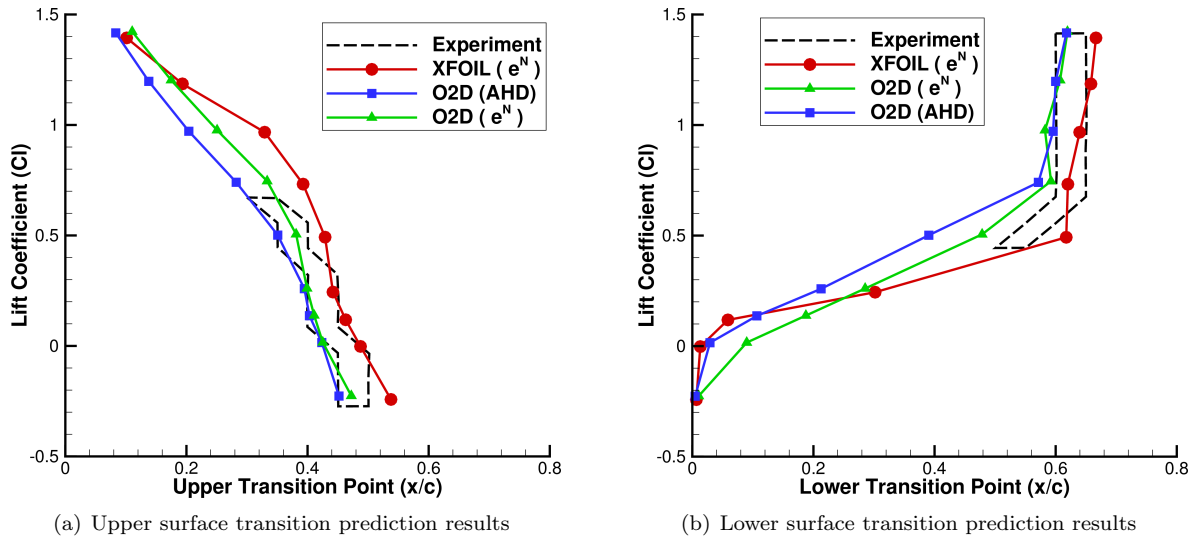


Figure 3. NLF-0416 transition prediction validation

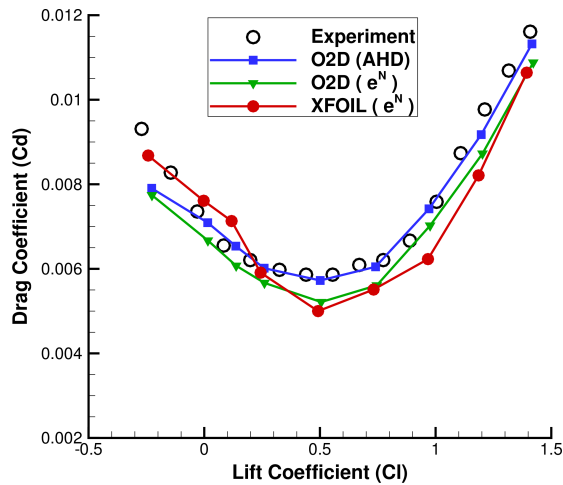


Figure 4. NLF-0416 drag polar comparison

### V.C. Optimization Results - Problem Definition

To demonstrate the NLF design capabilities of the optimization framework, lift-constrained drag minimization is performed under different flight conditions. The objective is to minimize the total drag of the airfoil constrained by a user-specified lift target,  $C_l^*$ . For structural considerations, additional inequality constraints are included. An area constraint ensures that the final area of the airfoil is greater than or equal to the initial area. A thickness constraint near the leading edge ensures a minimum thickness of 0.1% chord located at 0.5% chord.

The three flight conditions investigated, along with the specified lift target, are outlined in Table 1. The Reynolds and Mach numbers of Case C were selected to approximate the cruise flight conditions of the Dash-8 Q400 turboprop aircraft.

The initial geometry for all cases is the RAE-2822 parametrized by nineteen B-spline control points, as shown in Figure 5. The five control points nearest the trailing edge, as well as three co-linear control points located at the leading edge, are kept fixed throughout the optimization. The  $y$ -coordinates of the remaining ten control points are used as the geometric design variables (shaded in blue), with the angle of attack included as an additional design variable. The computational grid consists of a  $575 \times 224$  C-grid, resulting from grid convergence studies on the boundary-layer properties. Finally, all results were obtained using the compressible Bernoulli edge-finding method, the intermittency function transition region model, and a

Table 1. Optimization cases

Case	Reynolds Number ( $Re$ )	Mach Number ( $M$ )	Lift Target ( $C_l^*$ )
A	$5 \times 10^6$	0.2	0.2
B	$10 \times 10^6$	0.4	0.4
C	$15 \times 10^6$	0.6	0.4

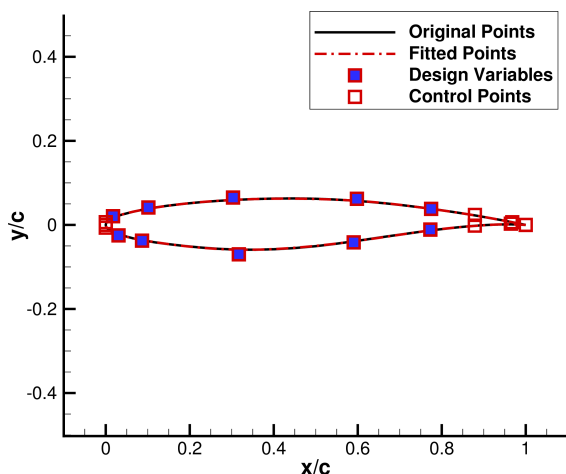


Figure 5. RAE-2822 b-spline parameterization

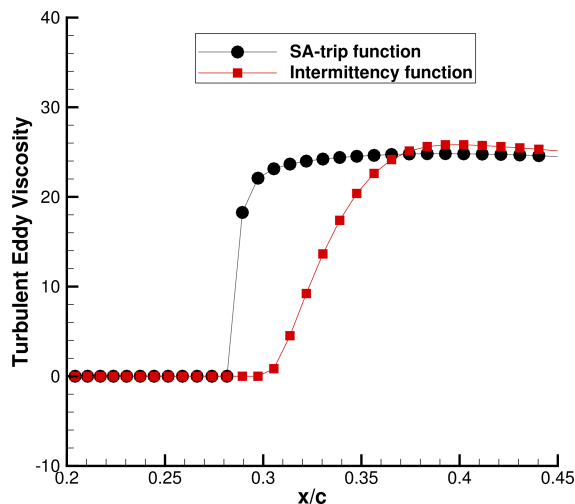


Figure 6. Eddy viscosity ramp-up on a NACA-0012 with transition at 30% chord

finite-difference gradient evaluation. Prior to discussing the optimization results, the next section presents a comparison of the transitional flow models.

#### V.D. Transitional Flow Models

The smoothness of the eddy viscosity ramp-up in the vicinity of the transition point was observed to have an impact on the smoothness of the design space and, in turn, the accuracy of the gradients. In this section, we compare the two transition region models discussed in Section III.D.2 by fixing the upper and lower transition points at 30 % chord on a NACA 0012 at  $Re=10 \times 10^6$ ,  $M=0.20$  and zero incidence, using a  $575 \times 224$  C-grid. Figure 6 shows the eddy viscosity ramp-up using both transition region models by following an upper surface grid line that is inside the boundary-layer. The SA model trip function was observed to sharply increase the eddy viscosity in the boundary-layer – typically one node upstream of the specified transition location<sup>41</sup> – whereas the intermittency function provides a smoother introduction of the eddy viscosity in accordance with the transition length (which in this case is fixed at 10% chord). The authors attempted a range of values for the constants  $c_{t1}$  and  $c_{t2}$  in the SA model trip functions;<sup>41</sup> however, no change in the sharp profile of the eddy viscosity was observed.

The sharp increase in the eddy viscosity observed when using the SA trip term was found to cause locally non-smooth design spaces for the grids typically employed for transition prediction. This becomes particularly evident when using a finite-difference approximation of the gradient, wherein small design changes result in variations of the transition points that are less than the distance between two streamwise nodes. A step-like noise in the design space was observed when under-resolving the SA model’s ramp-up. This noise is not present when using the more gradual S-curve intermittency function - indicative of a ramp-up that is sufficiently resolved by the fine grids typically required for transition prediction. As a result, the smoother intermittency function has been selected as the transition region model for this work.

Table 2. Case A summary of optimization results

	$C_d$	$C_l$	$C_m$	$T_{up}(x/c)$	$T_{lo}(x/c)$	$AoA$
Initial	0.00419	0.2001	-0.06842	0.6451	0.5174	-0.2278°
Final	0.00308	0.1991	-0.04525	0.7329	0.7430	0.1683°

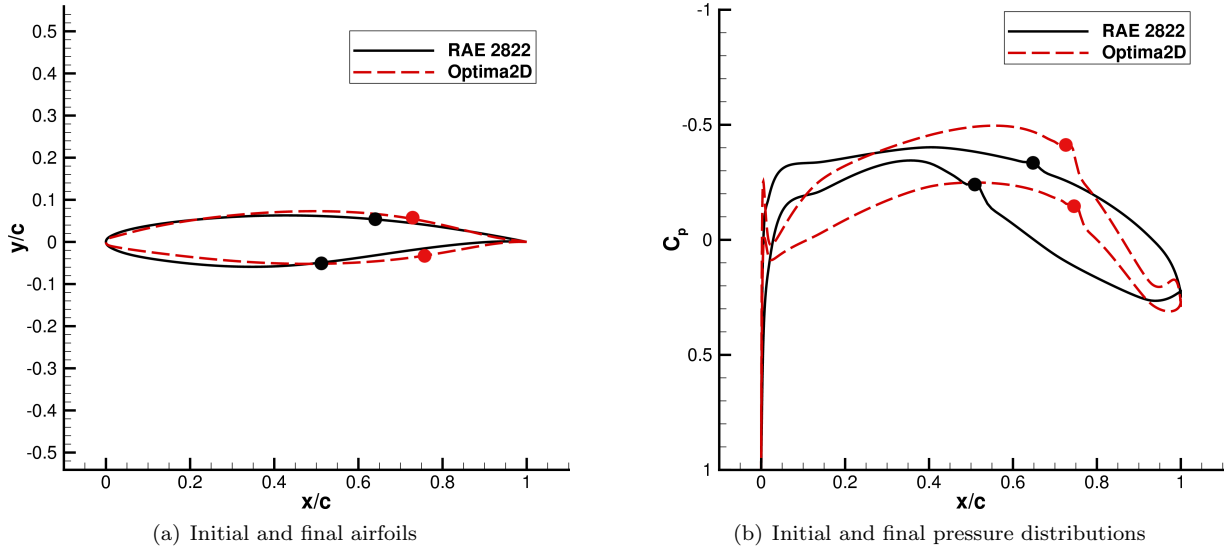


Figure 7. Case A optimization results;  $Re = 5 \times 10^6$ ,  $M = 0.2$ ,  $C_l^* = 0.2$ ; symbols indicate transition point locations

### V.E. Case A Results

The results for Case A were obtained using the  $e^N$  envelope transition criterion with  $N_{crit} = 9$ . Table 2 provides a summary of the results comparing the initial and final (optimized) airfoils. Figure 7(a) compares the initial and final geometries; Figure 7(b) compares the pressure profiles. The transition locations are indicated by the solid circles. The angle of attack was increased slightly from an initial value of  $-0.23^\circ$  to  $0.16^\circ$ , the lift target was achieved, and the total drag was reduced by 12 drag counts, or 26%. The ability of the optimizer to exploit the laminar-turbulent transition prediction is made evident by the aft movement of the transition points from 64% to 73% chord on the upper surface and 52% to 74% chord on the lower surface.

### V.F. CASE B Results

The results for Case B were obtained using the  $e^N$  envelope transition criterion with  $N_{crit} = 9$ . Table 3 provides a summary of the results comparing the initial and final (optimized) airfoils. The angle of attack was decreased from an initial value of  $1.28^\circ$  to  $0.85^\circ$ , the lift target was achieved, and the total drag was reduced by 15 drag counts, or 34%. The transition points on both the upper and lower surfaces were moved aft by approximately 20% chord.

Figure 8(a) compares the initial and final geometries; Figure 8(b) compares the pressure profiles. It can be observed that the optimizer was successful in designing an airfoil with an extended favourable pressure gradient on both the upper and lower surfaces. These results demonstrate the ability of the optimizer to design new NLF airfoils which would typically require considerable aerodynamic experience.

Table 3. Case B summary of optimization results

	$C_d$	$C_l$	$C_m$	$T_{up}(x/c)$	$T_{lo}(x/c)$	$AoA$
Initial	0.00438	0.3999	-0.07403	0.5150	0.5214	1.2831°
Final	0.00290	0.3998	-0.07897	0.7342	0.7256	0.8516°

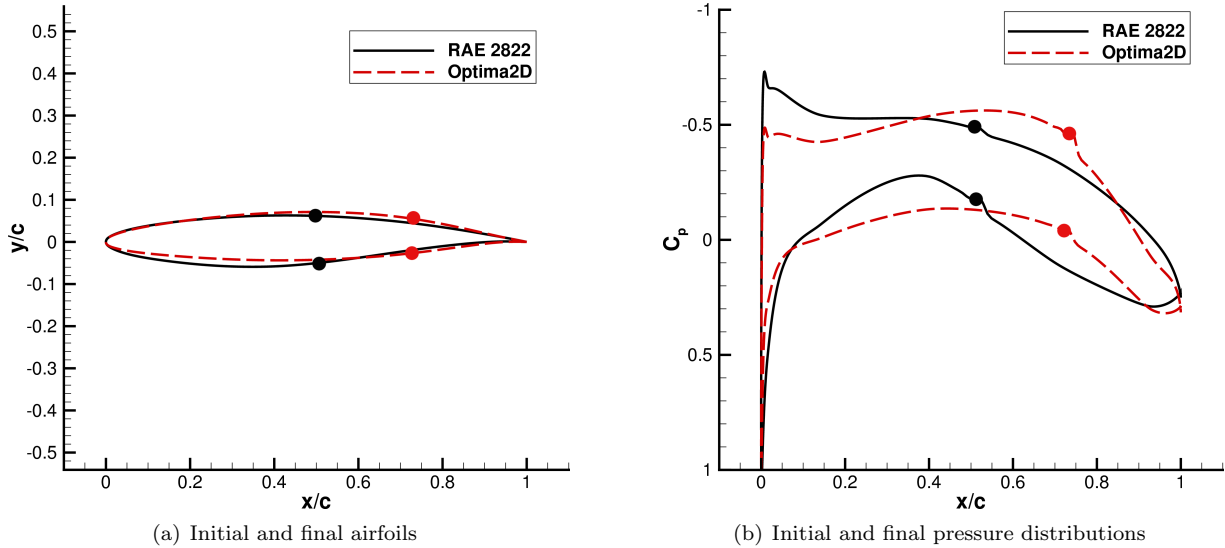


Figure 8. Case B optimization results:  $Re = 10 \times 10^6$ ,  $M = 0.4$ ,  $C_l^* = 0.4$ ; symbols indicate transition point locations

## V.G. CASE C Results

The results for Case C were obtained using the  $e^N$  envelope transition criterion with  $N_{crit} = 5$ . Table 4 provides a summary of the results comparing the initial and final (optimized) airfoils. The angle of attack was decreased from an initial value of 0.78° to 0.00°, the lift target was achieved, and the total drag was reduced by 7 drag counts, or 18%. The transition points on the upper surface were moved aft from 62% to 75% chord, and from 47% to 53% chord on the lower surface.

Figure 9(a) compares the initial and final geometries; Figure 9(b) compares the pressure profiles. Similar to the previous two cases, the optimizer was successful in designing an airfoil with extended regions of laminar flow on both the upper and lower surfaces, in turn, reducing the total drag.

## VI. Conclusions

A two-dimensional RANS solver making use of the Spalart-Allmaras turbulence model has been extended to incorporate an iterative laminar-turbulent transition prediction methodology. It was observed that with reasonable grid density sufficient accuracy of the boundary-layer properties can be computed directly from the Navier-Stokes solution. The compressible form of the AHD criterion and the simplified  $e^N$  envelope method have been implemented, verified, and validated by comparison to numerical and experimental data.

The RANS solver was subsequently employed in a gradient-based sequential quadratic programming shape optimization framework using the SNOPT optimization suite. A finite-difference gradient computation has been parallelized to enable a turn-around time equal to that of a single serial flow solve. The resulting optimization framework has been applied to the design of natural laminar flow airfoils. Such applications demonstrate the efficacy and practicality of using high-fidelity aerodynamic shape optimization as an NLF design tool. Future work will consider a new discrete-adjoint formulation for transition prediction in a RANS solver, as well as multipoint optimization to account for off-design performance, and the extension of the approach to three dimensions, incorporating a crossflow transition criterion.

Table 4. Case C summary of optimization results

	$C_d$	$C_l$	$C_m$	$T_{up}(x/c)$	$T_{lo}(x/c)$	$AoA$
Initial	0.00382	0.4000	-0.08620	0.6201	0.4651	$0.7756^\circ$
Final	0.00314	0.4000	-0.11606	0.7509	0.5346	$0.0024^\circ$

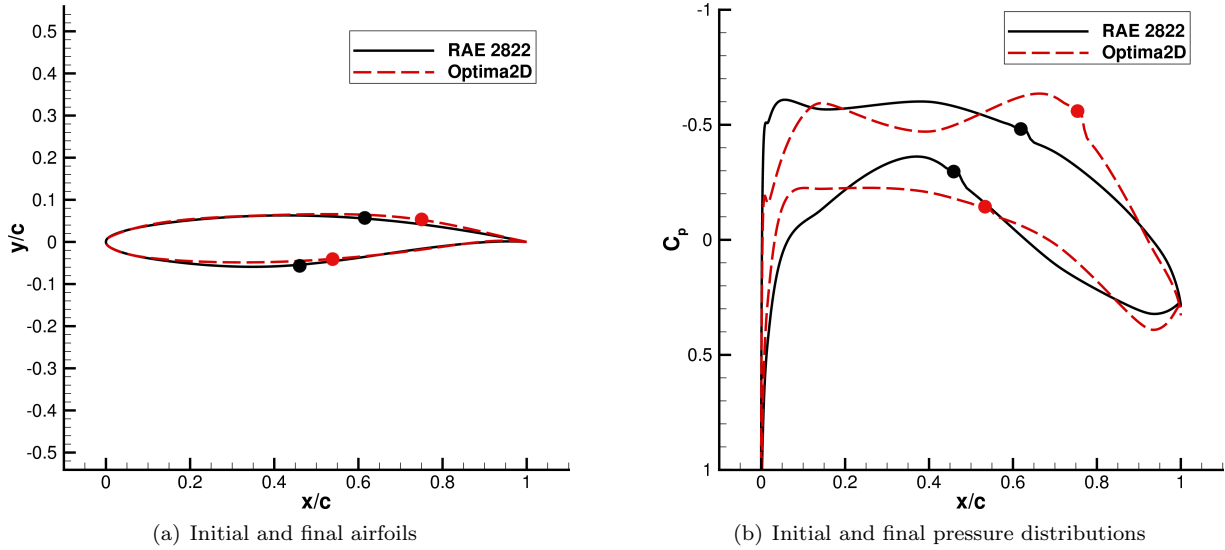


Figure 9. Case C optimization results:  $Re = 15 \times 10^6$ ,  $M = 0.6$ ,  $C_l^* = 0.4$ ; symbols indicate transition point locations

## VII. Acknowledgements

The authors gratefully acknowledge the financial assistance of the Ontario Government, Mathematics of Information Technology and Complex Systems, Canada Research Chairs Program, Bombardier Aerospace, and the University of Toronto.

## References

- <sup>1</sup>Marburger, J. H., "National Aeronautics Research and Development Plan," National Science and Technology Council, February 2010.
- <sup>2</sup>White, F. M., *Viscous Fluid Flow*, McGraw-Hill, Inc., 3rd ed., 2005.
- <sup>3</sup>Fujino, M., Yoshizaki, Y., and Kawamura, Y., "Natural-Laminar-Flow Airfoil Development for a Lightweight Business Jet," *Journal of Aircraft*, Vol. 40, No. 4, July-August 2003, pp. 609–615.
- <sup>4</sup>Campbell, R. L., Campbell, M. L., and Streit, T., "Progress Toward Efficient Laminar Flow Analysis and Design," *29th AIAA Applied Aerodynamics Conference*, No. AIAA–2011–3527, Honolulu, Hawaii, June 2011.
- <sup>5</sup>Kroo, I. and Sturdza, P., "Design-Oriented Aerodynamic Analysis for Supersonic Laminar Flow Wings," AIAA Paper 2003-0774, January 2003.
- <sup>6</sup>Brodeur, R. and van Dam, C., "Transition prediction for a two-dimensional Reynolds-Averaged Navier-Stokes method applied to wind turbine airfoils," *Wind Energy*, Vol. 4, No. 2, 2001, pp. 61–75.
- <sup>7</sup>Zingg, D. W. and Godin, P., "A perspective on turbulence models for aerodynamic flows," *International Journal of Computational Fluid Dynamics*, Vol. 23, No. 4, April-May 2009, pp. 327–335.
- <sup>8</sup>Reed, H. L. and Saric, W. S., "Transition Mechanisms for Transport Aircraft," *38th Fluid Dynamics Conference and Exhibit*, No. 2008-3743, Seattle, Washington, June 2008.
- <sup>9</sup>Arnal, D., Casalis, G., and Houdeville, R., "Practical Transition Prediction Methods: Subsonic and Transonic Flows," *VKI Lecture Series: Advances in Laminar-Turbulent Transition Modeling*, January 2009.
- <sup>10</sup>Krimmelbein, N., Nebel, C., and Radespiel, R., "Numerical Aspects of Transition Prediction for Three-Dimensional Configurations," *Fluid Dynamics and Co-located Conferences*, American Institute of Aeronautics and Astronautics, June 2005, pp. –.
- <sup>11</sup>Krumbein, A., " $e^N$  transition prediction for 3D wing configurations using database methods and a local, linear stability code," *Aerospace Science and Technology*, Vol. 12, No. 8, Dec. 2008, pp. 592–598.

- <sup>12</sup>Stock, H. W. and Haase, W., “Navier-Stokes Airfoil Computations with  $e^N$  Transition Prediction Including Transitional Flow Regions,” *AIAA Journal*, Vol. 38, No. 11, November 2000, pp. 2059–2066.
- <sup>13</sup>Stock, H. W. and Seitz, A., “Crossflow-Induced Transition Prediction Using Coupled Navier-Stokes and  $e^N$  Method Computations,” *AIAA Journal*, Vol. 42, No. 9, September 2004, pp. 1746–1754.
- <sup>14</sup>Nebel, C., Radespiel, R., and Wolf, T., “Transition Prediction for 3D Flows Using Reynolds-Averaged Navier-Stokes Code and N-factor Methods,” *33rd AIAA Fluid Dynamics Conference and Exhibit*, No. AIAA–2003–3593, Orlando, Florida, June 2003.
- <sup>15</sup>Cliquet, J., Houdeville, R., and Arnal, D., “Application of Laminar-Turbulent Transition Criteria in Navier-Stokes Computations,” *AIAA Journal*, Vol. 46, No. 5, May 2008, pp. 1182–1190.
- <sup>16</sup>Moens, F., Perraud, J., Krumbein, A., Toulorge, T., Iannelli, P., P., E., and Hanifi, A., “Transition prediction and impact on a three-dimensional high-lift-wing configuration,” *Journal of Aircraft*, Vol. 45, No. 5, May 2008, pp. 1751–1766.
- <sup>17</sup>Streit, T., Horstmann, H., Shraut, G., Hein, S., Fey, U., Egmai, Y., Perraud, J., Salah El Din, I., Cella, U., and Quest, J., “Complementary Numerical and Experimental Data Analysis of the ETW Telfona Pathfinder Wing Transition Tests,” *49th Aerospace Sciences Meeting and Exhibit*, No. AIAA–2011–881, Orlando, Florida, January 2011.
- <sup>18</sup>Mayda, E., *Boundary Layer Transition Prediction for Reynolds-Averaged Navier-Stokes Methods*, Ph.D. thesis, University of California, Davis, 2007.
- <sup>19</sup>Cebeci, T. and Cousteix, J., *Modeling and Computation of Boundary-Layer Flows*, Springer, Long Beach, 2nd ed., 2005.
- <sup>20</sup>Krumbein, A., “On Modeling of Transitional Flow and its Application on a High Lift Multi-Element Airfoil Configuration,” *41st Aerospace Sciences Meeting and Exhibit*, No. AIAA–2003–724, Reno, Nevada, January 2003.
- <sup>21</sup>Driver, J. and Zingg, D. W., “Numerical Aerodynamic Optimization Incorporating Laminar-Turbulent Transition Prediction,” *AIAA Journal*, Vol. 45, No. 8, August 2007, pp. 1810–1818.
- <sup>22</sup>Langtry, R. B. and Menter, F. R., “Transition Modeling for General CFD Applications in Aeronautics,” *43rd AIAA Aerospace Sciences Meeting and Exhibit*, No. AIAA–2005–522, Reno, Nevada, January 2005.
- <sup>23</sup>Langtry, R. B. and Menter, F. R., “Correlation-Based Transition Modeling for Unstructured Parallelized Computational Fluid Dynamics Codes,” *AIAA Journal*, Vol. 47, No. 12, December 2009, pp. 2894–2906.
- <sup>24</sup>Medida, S. and Baeder, J. D., “Application of the Correlation based  $\gamma$ - $Re_\theta$  Transition Model to the Spalart-Allmaras Turbulence Model,” *20th AIAA Computational Fluid Dynamics Conference*, No. AIAA–2011–3979, Honolulu, Hawaii, June 2011.
- <sup>25</sup>Aranake, A. C., Lakshminarayan, V. K., and Duraisamy, K., “Assessment of Transition Model and CFD Methodology for Wind Turbine Flows,” *42nd AIAA Fluid Dynamics Conference and Exhibit*, No. AIAA–2012–2720, New Orleans, Louisiana, June 2012.
- <sup>26</sup>Drela, M. and Giles, M. B., “Viscous-inviscid analysis of transonic and low Reynolds number airfoils,” *AIAA Journal*, Vol. 25, No. 10, 1987, pp. 1347–1355.
- <sup>27</sup>Krimmelbein, N. and Radespiel, R., “Transition prediction for three-dimensional flows using parallel computation,” *Computers & Fluids*, Vol. 38, No. 1, 2009, pp. 121–136.
- <sup>28</sup>Dodbele, S. S., “Design Optimization of Natural Laminar Flow Bodies in Compressible Flow,” Tech. Rep. 4478, National Aeronautics and Space Administration (NASA), Langley Field, VA., 1993.
- <sup>29</sup>Green, B. E., Whitesides, J. L., Campbell, R. L., and Mineck, R. E., “A Method for the Constrained Design of Natural Laminar Flow Airfoils,” AIAA Paper 96-2502, 1996.
- <sup>30</sup>Pralits, J., *Optimal Design of Natural and Hybrid Laminar Flow Control on Wings*, Ph.D. thesis, Royal Institute of Technology Department of Mechanics, Stockholm, Sweden, October 2003.
- <sup>31</sup>Amoignon, O., Berggren, M., Hanifi, A., Henningson, D., and Pralits, J., “Shape Optimization for Delay of Laminar-Turbulent Transition,” *AIAA Journal*, Vol. 44, May 2006, pp. 1009–1024.
- <sup>32</sup>Cameron, L., Early, J., and McRoberts, R., “Metamodel Assisted Multi-Objective Global Optimisation of Natural Laminar Flow Aerofoils,” *41st AIAA Fluid Dynamics Conference and Exhibit*, No. AIAA–2011–3001, Honolulu, Hawaii, June 2011.
- <sup>33</sup>Xu, J. and Kroo, I., “Aircraft Design with Active Load Alleviation and Natural Laminar Flow,” *53rd Structures, Structural Dynamics, and Materials and Co-located Conferences*, No. AIAA–2012–1428, Honolulu, Hawaii, April 2012.
- <sup>34</sup>Lee, J. and Jameson, A., “Natural-Laminar-Flow Airfoil and Wing Design by Adjoint Method and Automatic Transition Prediction,” *47th AIAA Aerospace Sciences Meeting and Exhibit*, No. AIAA–2009–897, Orlando, Florida, January 2009.
- <sup>35</sup>Khayatzaadeh, P. and Nadarajah, S., “Aerodynamic Shape Optimization via Discrete Viscous Adjoint Equations for the  $k$ - $\omega$  SST Turbulence and  $\gamma$ - $Re_\theta$  Transition Models,” *49th AIAA Aerospace Sciences Meeting and Exhibit*, No. AIAA–2011–1247, Orlando, Florida, January 2011.
- <sup>36</sup>Buckley, H. P. and Zingg, D. W., “An Approach to Aerodynamic Design through Numerical Optimization,” *AIAA Journal*, in press, January 2013.
- <sup>37</sup>Nemec, M. and Zingg, D. W., “Newton-Krylov algorithm for aerodynamic design using the Navier-Stokes Equations,” *AIAA Journal*, Vol. 40, No. 6, June 2002, pp. 1146–1154.
- <sup>38</sup>Nemec, M., Zingg, D. W., and Pulliam, T. H., “Multipoint and Multi-Objective Aerodynamic Shape Optimization,” *AIAA Journal*, Vol. 42, No. 6, June 2004, pp. 1057–1065.
- <sup>39</sup>Jameson, A., Schmidt, W., and Turkel, E., “Numerical solution of the Euler equations by finite volume methods using Runge-Kutta time-stepping schemes,” *14th AIAA Fluid and Plasma Dynamics Conference*, No. AIAA–81–1259, Palo Alto, California, June 1981.
- <sup>40</sup>Swanson, R. C. and Turkel, E., “On central-difference and upwind schemes,” *Journal of Computational Physics*, Vol. 101, No. 2, August 1992, pp. 292–306.
- <sup>41</sup>Spalart, P. R. and Allmaras, S. R., “A one-equation turbulence model for aerodynamic flows,” AIAA Paper 92-0439, January 1992.

<sup>42</sup>Stock, H.-W. and Haase, W., “Feasibility Study of  $e^N$  Transition Prediction in Navier-Stokes Methods for Airfoils,” *AIAA Journal*, Vol. 37, No. 10, October 1999, pp. 1187–1196.

<sup>43</sup>Arnal, D., Houdeville, R., Seraudie, A., and Vermeersh, O., “Overview of laminar- turbulent transition investigations at ONERA Toulouse,” *41st AIAA Fluid Dynamics Conference and Exhibit*, No. AIAA–2011–3074, Honolulu, Hawaii, June 2011.

<sup>44</sup>Krumbein, A., “Automatic Transition Prediction and Application to High-Lift Multi-Element Configurations,” *Journal of Aircraft*, Vol. 42, No. 5, 2005, pp. 1150–1164.

<sup>45</sup>Gill, P., Murray, W., and Saunders, M., “SNOPT: An SQP Algorithm for Large-Scale Constrained Optimization,” *SIAM Review*, Vol. 47, No. 1, 2005, pp. 99–131.

<sup>46</sup>Nocedal, J. and Wright, S. J., *Numerical Optimization*, Springer, 2nd ed., 2006.

<sup>47</sup>Somers, D. M., “Design and Experimental Results for a Natural-Laminar-Flow Airfoil for General Aviation Applications,” Technical Paper 1861, National Aeronautics and Space Administration, June 1981.

## Appendix: Details of Transition Criteria

In the compressible form of the AHD criterion, outlined in Section III.B, the functions  $A$  through  $F$  are computed as a function of the Mach number at the boundary-layer edge,  $M_e$ , as follows:<sup>43</sup>

$$\begin{aligned}
 A &= 98.64M_e^3 - 356.44M_e^2 + 117.13M_e - 236.69 \\
 B &= -13.04M_e^4 + 38.5M_e^3 - 30.07M_e^2 + 10.89M_e + 22.7 \\
 C &= 0.21M_e^3 + 4.79M_e^2 - 1.76M_e + 22.56 \\
 D &= -3.48M_e^4 + 6.26M_e^3 - 3.45M_e^2 + 0.23M_e + 12 \\
 E &= 0.6711M_e^3 - 0.7379M_e^2 + 0.167M_e + 51.904 \\
 F &= 0.3016M_e^5 - 0.7061M_e^4 + 0.3232M_e^3 - 0.0083M_e^2 - 0.1745M_e + 14.6
 \end{aligned}$$

In the simplified  $e^N$  envelope method, outlined in Section III.C, the functions  $\frac{dN}{dRe_\theta}$ ,  $m$ , and  $l$  are given as follows:<sup>26</sup>

$$\begin{aligned}
 \frac{dN}{dRe_\theta} &= 0.01 \sqrt{[2.4H_k - 3.7 + 2.5 \tanh(1.5H_k - 4.65)]^2 + 0.25} \\
 m(H_k) &= \left( 0.058 \frac{(H_k - 4)^2}{H_k - 1} - 0.068 \right) \frac{1}{l(H_k)} \\
 l(H_k) &= \frac{6.54H_k - 14.07}{H_k^2}
 \end{aligned}$$